Kinetics of intramolecular carbon atom exchange in ketene

Edward R. Lovejoy, Sang Kyu Kim, Ramón A. Alvarez, and C. Bradley Moore
Department of Chemistry, University of California at Berkeley, and Materials and Chemical Sciences Division of the Lawrence Berkeley Laboratory, Berkeley, California 94720

(Received 9 May 1991; accepted 6 June 1991)

Intramolecular carbon atom exchange in highly vibrationally excited ketene was studied by monitoring the carbon monoxide fragments (^{12}CO and ^{13}CO) from the photodissociation of $^{12}CH_2\,^{13}CO$ and $^{13}CH_2\,^{12}CO$. Two experimental techniques were employed. In one set of experiments the IR transient absorptions of ^{12}CO and ^{13}CO were measured following pulsed excimer excitation of ketene ^{13}C isotopomers, giving carbon atom exchange yields at 351 and 308 nm in a low pressure gas cell. In the other set of experiments, jet-cooled ketene ^{13}C isotopomers were excited with tunable near-UV radiation, and the CO products were detected by monitoring their VUV laser-induced fluorescence. Carbon atom exchange yields were measured for energies extending from below the triplet decomposition threshold ($CH_2CO \rightarrow CH_2(X\,^3B_1) + CO(X\,^1\Sigma^+)$) to about 4000 cm^{-1} above the singlet threshold ($CH_2CO \rightarrow CH_2(a\,^1A_1) + CO(X\,^1\Sigma^+)$). The exchange yields range from 4 to 19%, and the energy dependence of the yield exhibits pronounced structure, with maxima at the triplet and singlet decomposition thresholds. Kinetic measurements of the appearance of the CO products were also performed. The time constant for the appearance of the exchanged CO (e.g., ^{13}CO from $^{13}CH_2\,^{12}CO$) is significantly longer than that for the direct CO fragment (e.g., ^{12}CO from $^{13}CH_2\,^{12}CO$). All the experimental observations are consistent with a simple reaction mechanism involving ketene isomerization, $^{13}CH_2\,^{12}CO \rightleftarrows {}^{12}CH_2\,^{13}CO$, and dissociation, $^{13}CH_2\,^{12}CO \rightarrow {}^{13}CH_2 + {}^{12}CO$ and $^{12}CH_2\,^{13}CO \rightarrow {}^{12}CH_2 + {}^{13}CO$. The isomerization rate constant was determined by analyzing the CO kinetics and the carbon atom exchange yields in terms of the simple isomerization mechanism. A fit of the energy dependence of the isomerization rate constant to the results of tunneling-corrected Rice–Ramsberger–Kassel–Marcus (RRKM) calculations gave the threshold (28360 ± 60 cm^{-1}) for the isomerization process.

I. INTRODUCTION

The Wolff rearrangement is an important reaction step in the synthesis of carboxylic acids and esters, and is of fundamental interest because of the extensive bond rearrangements involved in the isomerization. The transformation is initiated by the decomposition of an α-diazo ketone, producing an oxo-carbene, which rearranges to the corresponding ketene.

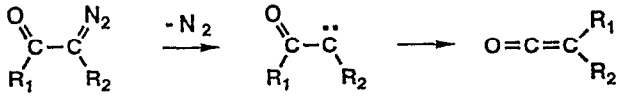

(1)

Ketenes react with water to form carboxylic acids, and with alcohols to produce esters. There has been a considerable amount of work aimed at understanding the mechanism of the Wolff rearrangement. Originally, it was believed that the ketene was formed by a simple migration of R_1 to the electron deficient carbon. However, carbon atom labeling experiments and chemical trapping studies suggest that the isomerization involves an oxirene intermediate which can undergo ring opening and R group migration in either direction.[1,2]

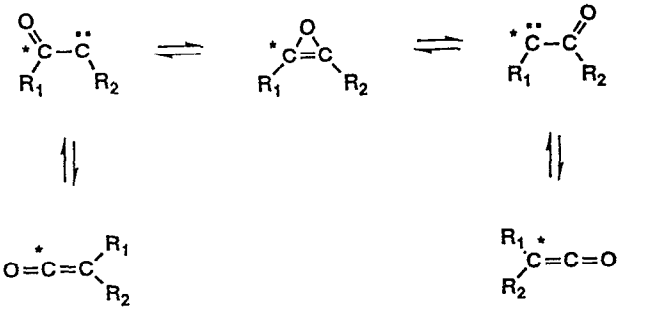

(2)

The ketene molecule, CH_2CO, is the simplest species ($R_1 = R_2 = H$) that can be involved in a Wolff-type isomerization reaction. Russell and Rowland[3] showed that highly excited ketene may also isomerize through an oxirene structure. They photolyzed ketene labeled at the methylene carbon and measured significant yields (about 5%–10%) of ^{14}CO at both 313 and 334 nm.

$$^{14}CH_2CO + h\nu \rightarrow CH_2 + {}^{14}CO. \qquad (3)$$

At 313 nm the first excited singlet state of methylene CH_2 ($a\,^1A_1$) is the dominant product, whereas at 334 nm the ground triplet state CH_2 ($X\,^3B_1$) is produced. Russell and Rowland proposed the following mechanism to explain the carbon atom exchange.

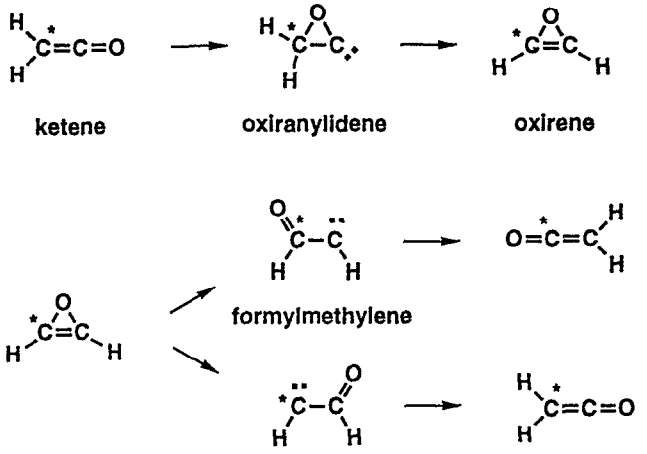

(4)

Montague and Rowland[4] also observed carbon exchange in the reaction of singlet methylene with CO.

$$^{14}CH_2\,(a\,^1A_1) + CO \rightarrow CH_2 + {}^{14}CO. \quad (5)$$

In a subsequent study, Zeller[5] reported carbon scrambling following photolysis of the simplest α-diazo compound, α-diazoacetaldehyde ($HCOCN_2H$). Zeller photolyzed ($\lambda > 220$ nm) α-diazoacetaldehyde labeled at the carbonyl carbon and trapped the ketene isotopomers with benzyl alcohol. ^{13}C nuclear magnetic resonance (NMR) and mass spectral analyses showed that 6–8% of the benzyl ester products contained the carbon label in the methyl position.

Theoretical calculations predict that the lowest energy pathway from ketene to oxirene is via a 1,2 H migration and O bridging.[6,7] The results of recent calculations for the energetics of the ketene/oxirene system are summarized in Fig. 1. The isomerization mechanism suggested by Russell and Rowland now appears to be unlikely due to a very high barrier ($\approx$120 kcal mol^{-1} above ground state ketene) separating oxiranylidene and ketene.[6] Both calculations summarized in Fig. 1 conclude that oxirene is stable. However, recent high level calculations by Vacek *et al.*[8] show that the frequency of the b_2 ring deformation mode of oxirene (which leads to formylmethylene) decreases unusually rapidly with the level of theory. Vacek *et al.* suggest that at higher levels of theory oxirene may be reduced to a transition state. The highest level of theory employed by Vacek *et al.* was the double zeta plus polarization (DZP) basis set, single and double excitation coupled cluster (CCSD) method. This is the highest level of theory that has been applied to calculations of the oxirene system. Vacek *et al.* were also unable to locate a transition state separating oxirene and formylmethylene, and found that formylmethylene was unstable. These calculations utilized the DZP basis set and configuration interaction wave functions which included single and double excitations (CISD).

The low lying electronic states of ketene are well characterized by *ab initio* studies.[9–11] The first excited singlet (S_1) and triplet (T_1) states are produced in a π–π^* type transition which weakens the π system resulting in elongation of the C–C bond and bending of the C–C–O framework. The

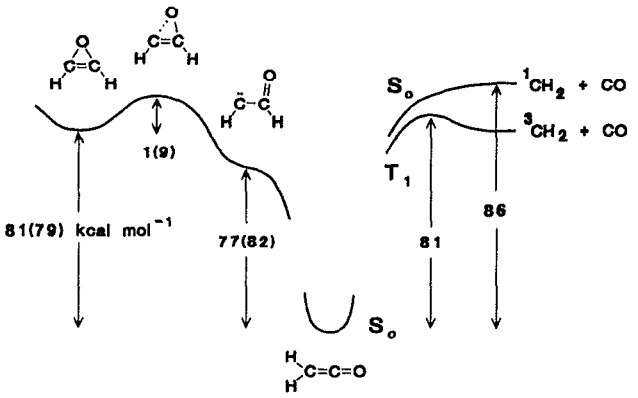

FIG. 1. *Ab initio* energies for C_2H_2O isomers relative to ground state ketene including zero point energies. The first energies are from calculations by Tanaka and Yoshimine (Ref. 7). These energies have been adjusted for zero point energies using values reported by Bouma *et al.* (Ref. 6). Tanaka and Yoshimine used a double zeta plus polarization basis set and configuration interaction wave functions which included all singly and doubly excited configurations. The energies in parentheses are from the calculations by Bouma *et al.* (Ref. 6) who employed a split valence plus *dp* polarization 6-31G** basis set with electron correlation included at the level of third-order Moller–Plesset perturbation theory. The ketene dissociation energies are experimental values from Chen *et al.* (Ref. 15) and Chen and Moore (Ref. 20).

first singlet absorption is weak ($\sigma_{max} \approx 3.5 \times 10^{-20}$ cm^2 molecule^{-1} at 320 nm)[12] and unstructured. The diffuse nature of the first singlet absorption[13] and the low quantum yield for fluorescence from the excited state are ascribed to rapid internal conversion from S_1 to highly vibrationally excited states of the ground state, S_0. Yoshimine[14] has located an accessible curve crossing near the excited state equilibrium geometry which would explain the high efficiency of the internal conversion process.

The S_1–S_0 transition is a convenient vehicle for preparing highly vibrationally excited ground state ketene due to the strong S_0/S_1 coupling, and the dynamics of ketene decomposition on the ground state singlet surface have been studied. Photofragment excitation (PHOFEX) spectra of the singlet methylene product show that there is no barrier to dissociation to singlet products and that the available energy is distributed statistically among the fragments.[15,16] Potter *et al.*[17] measured the unimolecular decay rate constants for the singlet dissociation for energies up to 5600 cm^{-1} above the threshold. The rate constants are fit very well with the variational Rice–Ramsberger–Kassel–Marcus (RRKM) theory of Klippenstein and Marcus,[18] but not with phase space theory.

Intersystem crossing (ISC) produces the first excited triplet state, and the dynamics of the triplet decomposition have been studied at energies below the singlet decomposition threshold. Measurements of CO rotational distributions[19] and unimolecular decomposition rate constants[20] indicate that there is a small barrier (about 1330 cm^{-1} above CH_2 ($X\,^3B_1$) + CO) in the exit channel which controls the decomposition dynamics on the triplet surface. The CO rota-

tional distributions are nonstatistical and are fit with a simple impulsive energy release model.

The unimolecular decompositions of ketene on the ground singlet and first excited triplet surfaces are well characterized due to the combination of detailed theoretical and experimental investigations. The dynamics of ketene dissociation are reconciled with the topology of the potential energy surfaces along the C–C coordinate past the transition states. However, *ab initio* calculations and carbon labeling experiments show that the highly vibrationally excited ketene molecule samples other very interesting portions of the C_2H_2O potential energy hypersurface.

In this work, isotopic labeling of ketene is used to sensitize the dissociation dynamics to portions of the C_2H_2O potential energy surface which have not been studied in any detail. The application of pulsed-jet and laser-based experimental techniques allows investigation of the photoinduced isomerization of ketene on the microcanonical level. Two experimental techniques are used to study the isomerization of ketene. In both studies, carbon monoxide photofragments are detected following near-UV excitation of ^{13}C isotopomers of ketene.

$$^{12}CH_2\,^{13}CO + h\nu \rightarrow {}^{12}CH_2 + {}^{13}CO \quad (6a)$$

$$\rightarrow {}^{13}CH_2 + {}^{12}CO, \quad (6b)$$

$$^{13}CH_2\,^{12}CO + h\nu \rightarrow {}^{13}CH_2 + {}^{12}CO \quad (7a)$$

$$\rightarrow {}^{12}CH_2 + {}^{13}CO. \quad (7b)$$

The extent of isomerization is related to the yield of the individual CO isotopomers. In one set of experiments, the CO fragments are detected by monitoring the transient absorbance of the output of an IR diode laser, following pulsed excimer laser excitation of isotopically labeled ketene in a low pressure cell. The second set of experiments employs tunable UV laser excitation of jet-cooled ketene and VUV LIF detection of the CO products.

This paper is arranged in the following order. First, the two experimental apparatuses and methodologies are described. Next, the results of carbon atom exchange yield experiments are presented, first for the IR apparatus, and then for the VUV LIF apparatus. A simple isomerization mechanism is proposed which explains the energy dependence of the exchange yield, and kinetic measurements designed to test the model are described. Finally, the kinetic parameters are compared with RRKM calculations based on *ab initio* results for the isomerization reaction coordinate.

II. EXPERIMENTAL

A. IR transient absorption

The details of the IR transient absorption apparatus used in this study have been published[21,22] and are not presented here. Briefly, the temporal evolution of carbon monoxide generated in the pulsed excimer photolysis (351 and 308 nm) of ketene was measured by monitoring the transient absorbance of a cw IR diode laser tuned to a specific rovibrational transition of the carbon monoxide.

Ketene carbon atom exchange yields were measured using two different approaches with the IR transient absorption apparatus. In one case, the ^{12}CO transient absorption signal ($R(11)$ or $R(13)$ (1–0)) from a natural ketene sample was measured to determine the total CO production from a specific pressure of ketene and for a specific UV laser fluence. Then, the photolysis cell was evacuated and flushed several times with He or N_2, and $^{12}CH_2\,^{13}CO$ was added to the same total pressure as used for the natural sample, and the ^{12}CO signal from the isotopically labeled compound was measured. In the absence of secondary chemistry, the exchange yield is the ratio of the ^{12}CO signal from the isotopically labeled ketene ($^{12}CH_2\,^{13}CO$) to that from the natural sample, minus a small contribution from isotopic impurities. The influence of CO production via secondary chemistry is discussed in the results section.

In the other experiments, both ^{12}CO and ^{13}CO were measured following pulsed photolysis of $^{13}CH_2\,^{12}CO$. The rovibrational transitions $P(16)$ (1–0) and $P(5)$ (1–0) were used to detect ^{12}CO and ^{13}CO, respectively. These transitions were used because (1) they were fully resolved from surrounding $^{13}CH_2\,^{12}CO$ features, (2) the transitions are separated by only 0.3 cm^{-1} and the diode laser was easily scanned between the lines, and (3) the line strength of the transition used to detect the minor fragment (^{13}CO $P(5)$) is near the maximum for thermalized CO at 300 K. For the $^{13}CH_2\,^{12}CO$ experiments, the reaction vessel was filled with 0.5–2.0 Torr of the labeled ketene and the diode laser was tuned to the peak of either the ^{12}CO or the ^{13}CO rovibrational feature. Transient absorbance profiles were averaged for 10–100 excimer shots. Then, the diode laser was tuned to the other CO isotopomer transition and more transient absorbance profiles were averaged. This sequence was repeated for up to 500 total laser shots per cell fill. In the absence of CO production via secondary chemistry, the carbon atom exchange yield for this experimental approach is simply the ratio of the CO absorbances (A) normalized to the respective line strengths (S).

$$\text{Yield} = \frac{A(^{13}CO)/S(^{13}CO)}{A(^{13}CO)/S(^{13}CO) + A(^{12}CO)/S(^{12}CO)}. \quad (8)$$

CO line strengths were taken from values reported by Chackerian *et al.* ($S(^{13}CO\ P(5)) = 8.31$ and $S(^{12}CO\ P(16)) = 2.97$ cm^{-2} atm^{-1} at 297 K).[23]

Equation (8) is valid if the CO product is thermalized when the absorption is measured. In this work, the CO signals were analyzed after at least 50 collisions ($t > 10$ μs, $P > 0.5$ Torr) which ensured that the CO was rotationally thermalized. Vibrational excitation of the CO fragment did not influence the data analysis since the ^{12}CO and ^{13}CO photofragments should have similar vibrational distributions and the degree of excitation is small at the energies used in these studies ($9 \pm 5\%$ $v = 1$ at 308 nm).[24]

B. Pulsed-jet/VUV LIF

The pulsed-jet/VUV LIF apparatus used in this work is similar to systems described by Butenhoff *et al.*[25] and Chen

and Moore.[20] Ar or He at 0.5 to 1.5 atm was bubbled through ketene cooled to 179 K (hexane slush, ketene vapor pressure $\approx$50 Torr), and the ketene/noble gas mixture was expanded through a pulsed nozzle (10 Hz repetition rate, $\approx$2 ms pulse duration, orifice diam 0.5 and 0.8 mm) into a low pressure chamber ($<5\times10^{-5}$ Torr) to produce rotationally cold ketene. The rotational temperature was not known but is estimated to be <10 K, based on an analysis of CH_2O LIF spectra for similar expansion conditions.

The cold ketene was excited in the wavelength region from about 300 to 350 nm with the frequency-doubled output of a Nd:YAG-pumped dye laser. This laser system produced UV pulses ($\approx$7 ns duration) with energies from 3 to 10 mJ pulse^{-1} ($\approx$20 mm^2 cross section) and a bandwidth of about 0.3 cm^{-1}. The visible light was generated with mixtures of LDS 698 and DCM laser dyes in methanol, and the frequency was calibrated to an accuracy of $\pm$0.5 cm^{-1} using Ne optogalvanic transitions. The UV light was separated from the fundamental visible light during 3 reflections from dichroic mirrors before entering the vacuum chamber.

The probe laser system was a Nd:YAG-pumped dye laser with an output energy of 10–20 mJ pulse^{-1} at 435 nm (Coumarin 440 dye in methanol). The laser beam had a cross section of about 8 mm^2 and an approximate bandwidth of 0.1 cm^{-1}. The blue light was focussed (8 cm focal length quartz lens) at the center of a cell containing 20–40 Torr of Xe to produce the third harmonic frequency. The efficiency of the tripling process is estimated to be about 10^{-6}.[26] The probe laser beam was collimated (8 or 10 cm focal length CaF_2 lens) at the exit of the tripling cell and crossed the jet expansion 1–2 cm below the nozzle. The VUV laser radiation excited CO rovibronic transitions in the ($A\,^1\Pi$–$X\,^1\Sigma^+$) (3–0) band. The laser excited fluorescence was viewed with a photomultiplier tube (PMT) mounted horizontally, mutually orthogonal to the laser beams and the axis of the jet expansion. A cultured quartz window (2.5 mm thick, $\approx$50% transmission at 150 nm) and a 2.5 cm diam CaF_2 $f/1$ lens were positioned in front of the PMT to attenuate scattered VUV laser light and to increase the photon collection efficiency.

The UV excitation laser was polarized vertically, parallel with the axis of the jet expansion, and propagated collinearly and opposite to the probe laser pulse. The probe laser was polarized horizontally, perpendicular to both the jet axis and the UV excitation polarization. A portion of the VUV laser radiation was reflected onto another VUV sensitive PMT by an LiF beamsplitter located in the sidearm of the vacuum chamber, opposite to the tripling cell. The signal from this detector was used to normalize for the $\pm$20% shot-to-shot variation in the VUV laser output. Fluctuations in the UV laser output were monitored with a fast photodiode which detected the light scattered from the Brewster window at the entrance to the vacuum chamber. Scattered visible radiation was blocked with a filter placed in front of the photodiode.

The linearity of the normalization techniques was checked by varying the UV and VUV intensities while monitoring the CO LIF signal. The UV intensity was attenuated by placing glass slides nearly normal to the laser beam. The overlap of the excitation and probe laser beams was optimized for each intensity level to compensate for the beam displacement caused by the slides. The VUV intensity was varied by changing the Xe pressure in the tripling cell. For both normalization schemes, the ketene CO LIF signal varied linearly with the normalization signal for eightfold decreases in the laser intensities below typical operating levels. The amplified (100 times) CO LIF signal and the two laser normalization signals were sampled with boxcars. The boxcar outputs were digitized and processed with a microcomputer, which also controlled the laser scanning.

Two types of experiments were performed with the pulsed-jet/VUV LIF apparatus. In one set of experiments, ^{12}CO and ^{13}CO LIF spectra were collected to measure the fraction of carbon atom exchange at specific ketene excitation energies. Typically, the VUV laser was stepped about 0.1 cm^{-1} and the signals from 5–20 laser firing sequences (excitation + probe) were averaged at each step. The time delay between the lasers was set to between 100 and 3000 ns. The CO spectra exhibited a linewidth of about 0.5 cm^{-1} (full width at half-maximum) which is a convolution of the VUV laser bandwidth ($\approx$0.2–0.3 cm^{-1}) and Doppler broadening dominated by the spread of ketene velocities in the jet expansion.

The pulsed-jet/VUV LIF apparatus was also used to measure the temporal evolution of the ^{12}CO and ^{13}CO photofragments. Two experimental approaches were employed. In one set of experiments, the time delay between the UV excitation and the VUV probe lasers was scanned with a programmable time delay generator while the VUV laser frequency was fixed on the peak of a CO rovibronic transition [usually $Q(12)$]. One hundred to 300 delay times were sampled per scan ($t_{max}<1\,\mu$s), and 10–50 scans were averaged. In the other experimental approach, the time delay was stepped manually and at each delay the probe laser was scanned over adjacent ^{12}CO and ^{13}CO LIF features. For most of the experiments, ^{12}CO $P(15)$ and ^{13}CO $Q(12)$, which were completely resolved and separated by only 3.5 cm^{-1}, were used. The reaction time was measured by monitoring the scattered light from both lasers at the exit window of the vacuum chamber with a fast photodiode and an oscilloscope. The measured time delay was corrected for an offset due to the transit time of the light pulses between the nozzle and the photodiode ($\approx$10 ns).

C. Ketene ^{13}C isotopomer synthesis and purity

Ketene was prepared by the pyrolysis of acetic anhydride in a red-hot quartz tube, and purified by trap-to-trap distillations from 142 K (*n*-pentane slush) to 77 K (liquid N_2). The ketene isotopomers, $^{12}CH_2\,^{13}CO$ and $^{13}CH_2\,^{12}CO$, were synthesized from acetic anhydride-1, $1'^{13}C_2$ and acetic anhydride-2,$2'^{13}C_2$ (minimum 99% ^{13}C), respectively. FTIR and mass spectral analyses of the ketene products revealed small quantities (1–2%) of $^{12}CH_2\,^{12}CO$ and $^{13}CH_2\,^{13}CO$ in both samples. A small ^{18}O enrichment (1–3% ^{18}O) was also detected in the $^{12}CH_2\,^{13}CO$ sample.

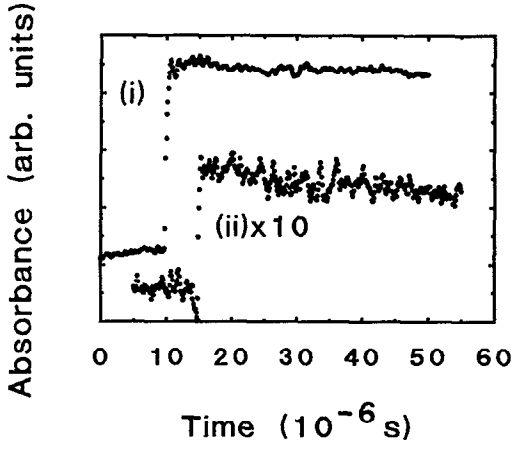

FIG. 2. Transient absorbance of ^{12}CO $R(11)$ (1-0) following excimer laser photolysis (351 nm, 9 mJ cm^{-2} pulse^{-1}) of (i) 1.00 Torr CH_2CO with a natural isotopic composition and (ii) 1.00 Torr $^{12}CH_2{}^{13}CO$. The time scales for the two traces are offset by 5 μs for clarity.

III. RESULTS AND DISCUSSION

A. IR transient absorption experiments

Ketene photodissociation at 351 nm produces only the triplet ground state of methylene due to energy restraints.

$$CH_2CO + h\nu(351\ \text{nm}) \rightarrow CH_2(X\,^3B_1) + CO. \quad (9)$$

Triplet methylene reacts slowly with ketene ($k < 2\times10^{-15}$ cm^3 molecule^{-1} s^{-1})[27] and was not an important source of CO on the time scale of our experiments ($t < 50$ μs). The self-reaction of triplet methylene

$$CH_2(X\,^3B_1) + CH_2(X\,^3B_1) \rightarrow C_2H_2 + H_2(2H), \quad (10)$$

which may produce hydrogen atoms, did not lead to significant CO production on the time scale of our experiments, since the initial triplet methylene concentration was less than 2×10^{13} molecule cm^{-3}. Therefore, at 351 nm the CO signals reflected only the unimolecular decay channel of ketene.

The carbon atom exchange yield at 351 nm was measured using both techniques discussed in the experimental section, first by comparison of the ^{12}CO production from $^{12}CH_2{}^{13}CO$ with that from unlabeled ketene, and second by measurement of both ^{12}CO and ^{13}CO from $^{13}CH_2{}^{12}CO$. A set of transient absorption profiles for the first method are shown in Fig. 2. The results of measurements using both approaches are summarized in Table I.

Ketene photodissociation at 308 nm produces predominately singlet methylene (> 80%), and only a small fraction of the triplet ground state.[28,29]

$$CH_2CO + h\nu(308\ \text{nm}) \rightarrow CH_2(a\,^1A_1) + CO \quad (11a)$$

$$\rightarrow CH_2(X\,^3B_1) + CO. \quad (11b)$$

Singlet methylene reacts very rapidly with ketene ($k = 2.7\times10^{-10}$ cm^3 molecule^{-1} s^{-1})[30] and produces CO.

$$CH_2(a\,^1A_1) + CH_2CO \rightarrow C_2H_4 + CO \quad (12a)$$

$$\rightarrow CH_2(X\,^3B_1) + CH_2CO. \quad (12b)$$

The CO yield in reaction (12) is about 60%,[22] and for the ketene pressures used in this work (> 0.5 Torr), reaction (12) was > 90% complete during the risetime ($\tau \approx 150$ ns) of the transient absorption signal. Consequently, the production of CO in reaction (12) had to be considered when calculating the carbon exchange yield from the CO signals. Assuming that the methylene chemistry does not scramble the carbon labels, i.e., the reaction

$$^{12}CH_2 + {}^{12}CH_2{}^{13}CO \rightarrow {}^{12}CH_2{}^{13}CH_2 + {}^{12}CO \quad (13)$$

TABLE I. Carbon atom exchange yields measured with the excimer photolysis/IR absorption apparatus.

$[^{12}CH_2{}^{13}CO]$ (Torr)	$[^{13}CH_2{}^{12}CO]$ (Torr)	$[N_2]$ (Torr)	$[i-C_4H_8]$ (Torr)	Excitation λ (nm)	Excitation (mJ)	Detection ^{12}CO	Detection ^{13}CO	Yield[a] (%)
1.00				351	9	$R(11)$		6.0(4)
0.51				351	9	$R(11)$		7.1(6)
0.46				351	9	$R(11)$		6.8(7)
1.00		2.20		351	9	$R(11)$		7.6(7)
1.00		8.20		351	9	$R(11)$		6.6(9)
2.13				351	9	$R(11)$		6.3(7)
1.01				351	5	$R(13)$		5.3(9)
1.01				351	20	$R(13)$		5.7(7)
	1.01			351	11	$P(16)$	$P(5)$	6.8(9)
	1.01			351	11	$P(16)$	$P(5)$	6.5(8)
	0.81			351	10	$P(16)$	$P(5)$	6.5(7)
	0.81			351	5	$P(16)$	$P(5)$	7.3(10)
0.51				308	10	$R(11)$		6.7(6)
0.51			8.8	308	10	$R(11)$		5.7(8)
0.97				308	10	$R(11)$		7.1(8)
0.97			9.0	308	10	$R(11)$		6.1(4)

[a] The yields are not corrected for impurities ($1.0 \pm 0.5\%$) in the ketene isotopomer samples. One standard deviation is shown in parentheses.

is not important, the yield for C atom exchange in the photodissociation of $^{12}CH_2\,^{13}CO$ is given by

$$Y=\frac{[^{12}CO]_1}{[^{12}CO]_2/(1+X)}, \tag{14}$$

where the subscript 1 denotes $^{12}CH_2\,^{13}CO$ photolysis and 2 refers to experiments using an equal pressure of ketene with a natural isotopic composition. $[^{12}CO]$ is proportional to the IR absorbance at $10\,\mu s < t < 50\,\mu s$ for the ketene concentrations used in this work. X is the product of the quantum yield for singlet methylene production from ketene at 308 nm (0.9 ± 0.1)[28,29] and the yield of CO in reaction (12) (0.6 ± 0.2).[22]

To check for complications due to singlet methylene chemistry, several experiments were performed in the presence of an excess of isobutylene (i-C_4H_8), which reacts very rapidly with singlet methylene.

$$CH_2(a\,^1A_1) + i\text{-}C_4H_8 \rightarrow \text{products} \tag{15}$$

($k = 2.3\times10^{-10}$ cm^3 molecule^{-1} s^{-1}).[30] For large ratios of isobutylene to ketene, the CO production via CH_2 ($a\,^1A_1$) chemistry should be negligible, and the exchange yield will be given simply by the ratio of the ^{12}CO from $^{12}CH_2\,^{13}CO$ to that from unlabeled ketene [Eq. (14) with $X = 0$].

Carbon atom exchange yields measured with isobutylene to ketene ratios of 9 and 17 were in good agreement with the results corrected for secondary CO production in the absence of isobutylene. The yields measured at 308 nm are listed in Table I along with the 351 nm results. The yields at both wavelengths appear to be independent of the bath gas identity (N_2, i-C_4H_8), cell pressure (0.5–10 Torr), ketene isotopomer ($^{12}CH_2\,^{13}CO$, $^{13}CH_2\,^{12}CO$), CO rovibrational transition ($R(11)$ and $R(13)$), and photolysis laser fluence (5–20 mJ cm^{-2}). Weighted ($1/\sigma^2$) averages of the data in Table I give uncorrected exchange yields of $6.5 \pm 0.4\%$ at 351 nm and $6.4 \pm 1.4\%$ at 308 nm, where the uncertainties are the 95% confidence limits for the precision. Correction for isotopic impurities in both ketene samples of $1.0 \pm 0.5\%$ gives absolute carbon atom exchange yields equal to $5.5 \pm 0.6\%$ at 351 nm and $5.4 \pm 1.5\%$ at 308 nm.

The accuracy of the yield measurements was checked by measuring the ^{13}CO yield from unlabeled ketene at 351 nm. Two separate sets of measurements gave ^{13}CO yields of $1.6 \pm 0.8\%$ and $1.3 \pm 0.6\%$ where the uncertainties are 95% confidence limits for precision derived from 4 measurements. These values are in good agreement with the natural abundance of the $^{12}CH_2\,^{13}CO$ isotopomer (1.1%).

B. Pulsed-jet/VUV LIF experiments

A more complete study of the energy dependence of the carbon atom exchange yield was performed with the pulsed-jet/VUV LIF apparatus. These experiments have some important advantages relative to the excimer laser photolysis/IR transient absorption studies. (1) The uncertainty in the energy of the ketene molecule is decreased significantly by using a narrow bandwidth excitation laser and supersonic-jet cooling of the ketene. (2) The unimolecular chemistry can be studied in the absence of collisions, and (3) a more extensive study of the energy dependence of the isomerization reactions can be performed with the continuously tunable excitation source.

1. ^{12}CO and ^{13}CO rotational distributions

Kim *et al.*[29] have shown that the rotational distributions of the CO produced in ketene photodissociation at energies just above the singlet threshold are bimodal, with a low-J component due to the CO from the singlet channel and a broader component at high J from the CO associated with the triplet channel. In this work, the LIF excitation spectra of the ^{12}CO and ^{13}CO fragments from the photolysis of $^{12}CH_2\,^{13}CO$ were measured at 30 217 cm^{-1}, about 100 cm^{-1} above the singlet decomposition threshold of $^{12}CH_2\,^{12}CO$. The purpose of these experiments was to compare the rotational distributions of the two different CO products at an energy where ketene dissociation gives a very characteristic CO rotational signature.

The rotational state populations were calculated from the measured LIF intensities using the relationship derived by Greene and Zare.[31] The details of the analysis for ketene photodissociation have been described by Chen and Moore[19] and Kim *et al.*,[29] and are not discussed here.

The ^{12}CO and ^{13}CO rotational distributions from the photolysis of $^{12}CH_2\,^{13}CO$ at 30 217 cm^{-1} are shown in Fig. 3. Each point is the average of populations calculated from resolved P, Q, and R branch lines for two scans of the spectra. The ^{12}CO populations were calculated with fewer lines than for ^{13}CO because a significant portion of the ^{12}CO LIF spectrum was overlapped by the more intense ^{13}CO spec-

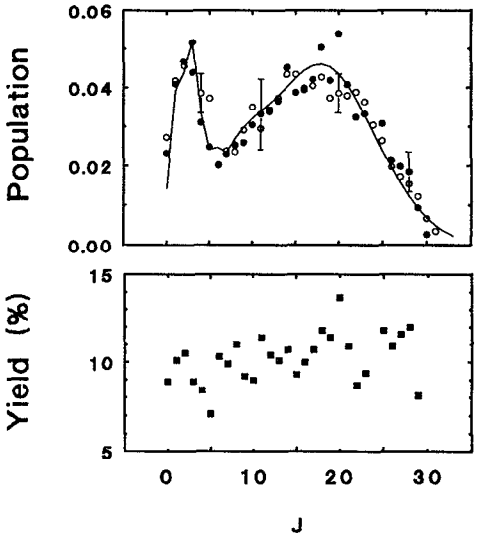

FIG. 3. ^{13}CO (○) and ^{12}CO (●) rotational distributions from the photolysis of $^{12}CH_2\,^{13}CO$ at 30 217 cm^{-1} with a 200 ns time delay between ketene excitation and CO detection. The error bars are 95% confidence intervals for precision. The solid line is a fit of the data to the sum of a singlet distribution given by phase space theory and a Gaussian-shaped triplet distribution (Ref. 29). The lower figure is the ^{12}CO yield as a function of the rotational quantum number.

trum. No correction was made for the contribution of the underlying ^{12}CO lines to the ^{13}CO population calculation, which may explain some of the scatter in the populations and yields.

The ^{12}CO and ^{13}CO fragments have similar rotational distributions which suggests that both fragments dissociate from highly vibrationally excited ketene. However, the distributions are expected to be slightly different due to differences in dissociation threshold energies for $^{12}CH_2\,^{13}CO$ and $^{13}CH_2\,^{12}CO$. These differences arise from the variation of the zero point energies of the reactant and transition state with isotopic composition. Zero point energies and dissociation thresholds for ketene isotopomers important in this work are listed in Table II. Vibrational frequencies were calculated using experimental and *ab initio* force fields for ground state ketene[32] and the transition states.[33] The zero point energy calculations show that the singlet threshold energy of $^{12}CH_2\,^{13}CO$ is about 10 cm^{-1} below that of $^{13}CH_2\,^{12}CO$. The small change in CO rotational excitation associated with a 10 cm^{-1} difference in available energy is not discernable in this work.

Kim *et al.*[29] have demonstrated that the rotational distributions from singlet ketene are described accurately by phase space theory. In contrast, the triplet dissociation produces nonstatistical rotational energy release and the J distributions are nearly Gaussian in shape.[19] Kim *et al.* measured singlet/triplet branching ratios at energies just above the singlet threshold by deconvoluting the bimodal rotational distributions. The data analysis was based on fitting the observed distribution to the sum of a phase space prediction for the singlet channel and a Gaussian distribution for the triplet product. The solid line shown in Fig. 3 is the ^{13}CO distribution calculated by using the analysis developed by Kim *et al.* and a singlet channel yield of 17%. The energy available to the singlet products (77 cm^{-1}) was determined from the known threshold for $^{12}CH_2\,^{12}CO$ [15] and zero point energy calculations for $^{12}CH_2\,^{13}CO$ (see Table II). The calculated ^{12}CO rotational distribution is similar to the ^{13}CO distribution (maximum deviation $<10\%$) and is not shown. Both calculated distributions are in good agreement with the experimental data.

2. Carbon atom exchange yield as a function of energy

Carbon atom exchange yields were measured as a function of J at specific excitation energies by comparing the LIF spectra of the ^{12}CO and ^{13}CO photofragments. A portion of the CO (A–X) (3–0) LIF spectrum taken 340 ns after $^{13}CH_2\,^{12}CO$ excitation at 28 450 cm^{-1} is shown in Fig. 4 to illustrate the signal levels and the spectral resolution. A direct comparison of the LIF intensities of the same rotational transitions for the ^{12}CO and ^{13}CO fragments gives the relative populations of the rotational states for the two frag-

TABLE II. Calculated zero point energies and dissociation threshold energies for ketene ^{13}C isotopomers.

Isotopomer[a]	Zero point energy (cm^{-1})
$^{12}CH_2\,^{12}CO(X\,^1A_1)$	6723
$^{13}CH_2\,^{12}CO(X\,^1A_1)$	6689
$^{12}CH_2\,^{13}CO(X\,^1A_1)$	6678
$^{13}CH_2\,^{13}CO(X\,^1A_1)$	6643
$^{12}CH_2\,^{12}CO(^3A'')^{\ddagger}$	5682
$^{13}CH_2\,^{12}CO(^3A'')^{\ddagger}$	5666
$^{12}CH_2\,^{13}CO(^3A'')^{\ddagger}$	5656
$^{13}CH_2\,^{13}CO(^3A'')^{\ddagger}$	5641
$^{12}CH_2(a\,^1A_1) + {}^{12}CO(X\,^1\Sigma^+)$	4584
$^{13}CH_2(a\,^1A_1) + {}^{12}CO(X\,^1\Sigma^+)$	4573
$^{12}CH_2(a\,^1A_1) + {}^{13}CO(X\,^1\Sigma^+)$	4560
$^{13}CH_2(a\,^1A_1) + {}^{13}CO(X\,^1\Sigma^+)$	4549
Reaction	**Relative threshold energy (cm^{-1})**
$^{12}CH_2\,^{12}CO(X\,^1A_1) \rightarrow {}^{12}CH_2(a\,^1A_1) + {}^{12}CO(X\,^1\Sigma^+)$	0
$^{13}CH_2\,^{12}CO(X\,^1A_1) \rightarrow {}^{13}CH_2(a\,^1A_1) + {}^{12}CO(X\,^1\Sigma^+)$	+23
$^{12}CH_2\,^{13}CO(X\,^1A_1) \rightarrow {}^{12}CH_2(a\,^1A_1) + {}^{13}CO(X\,^1\Sigma^+)$	+21
$^{13}CH_2\,^{13}CO(X\,^1A_1) \rightarrow {}^{13}CH_2(a\,^1A_1) + {}^{13}CO(X\,^1\Sigma^+)$	+45
$^{12}CH_2\,^{12}CO(^1A_1) \rightarrow {}^{12}CH_2\,^{12}CO(^3A'')^{\ddagger}$	0
$^{13}CH_2\,^{12}CO(^1A_1) \rightarrow {}^{13}CH_2\,^{12}CO(^3A'')^{\ddagger}$	+18
$^{12}CH_2\,^{13}CO(^1A_1) \rightarrow {}^{12}CH_2\,^{13}CO(^3A'')^{\ddagger}$	+19
$^{13}CH_2\,^{13}CO(^1A_1) \rightarrow {}^{13}CH_2\,^{13}CO(^3A'')^{\ddagger}$	+39

[a] $(^3A'')^{\ddagger}$ is the C_s^{II} (DZP CISD) triplet dissociation transition state described by Allen and Schaefer (Ref. 33).

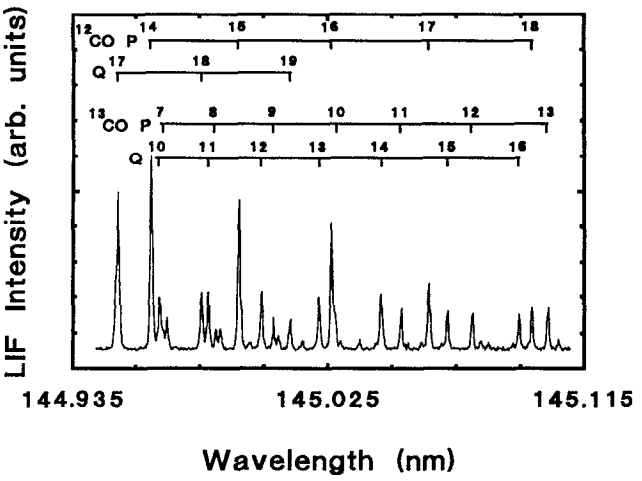

FIG. 4. A portion of the carbon monoxide (A-X) (3-0) LIF spectrum taken 340 ns after photoexcitation of $^{13}CH_2\,^{12}CO$ at 28 450 cm^{-1}. Assignments for the weaker R branch lines are not shown.

ments, since the ^{12}CO and ^{13}CO Franck–Condon factors are essentially the same [0.181 and 0.183, respectively, for the (A–X) (3–0) band][34] and the other intensity factors depend only on J'' and J'. Usually, spectra encompassing 7–30 different transitions common to both CO species were measured and the carbon atom exchange yield was calculated for each transition. In some cases, the intensities of unresolved clusters of lines near the bandheads of ^{12}CO and ^{13}CO were compared. There was no systematic variation in the yield as a function of J for any of the photolysis energies used, suggesting that the CO fragments have similar rotational energy distributions over the wide range of excitation energies used in this study (28 250–34 100 cm^{-1}).

The delay between ketene excitation and measurement of the photofragment spectra was set to where the yield was no longer increasing with time. Measurements of the temporal evolution of the exchange yield are discussed in the next section.

The carbon atom exchange yields measured with the pulsed-jet apparatus are listed in Table III, and are plotted as a function of energy in Fig. 5. There is very good agreement between the IR transient absorption gas cell experiments and the pulsed-jet results. The precision of the yield calculated from a set of rotational lines for one scan of the ^{12}CO and ^{13}CO spectra was typically about 15% of the mean at the 95% confidence level. One or two spectra were analyzed at each energy. The variation of the yield from spectrum to spectrum at a specific energy was usually less than $\pm$ 20% of the yield.

The exchange yields measured by Russell and Rowland[3] for $^{14}CH_2CO$ photodissociation at 313 and 334 nm are also shown in Fig. 5. Their results are in excellent agreement with the present work.

3. Ketene isomerization mechanism

Rate constants for ketene unimolecular decomposition reported in the literature[17,20,29] are plotted as a function of

TABLE III. Carbon atom exchange yields measured with the pulsed-jet/VUV LIF apparatus.

Energy (cm^{-1})	Δt[a] (μs)	Ketene isotopomer[b]	J_{CO} range[c]	Yield[d] (%)
28 250	3.00	*B*	9–16	12.3(2.1)
28 300	3.00	*B*	11–16	15.9(2.9)
28 300	3.00	*B*	11–16	15.9(1.8)
28 450	0.34	*B*	9–16	13.7(1.7)
28 450	0.66	*B*	11–16	11.6(1.7)
28 500	0.50	*B*	11–16	8.2(1.1)
28 600	0.20	*B*	11–16	5.3(1.3)
28 600	0.13	*B*	8–18	7.2(1.2)
28 700	0.20	*B*	11–16	5.3(1.3)
28 800	0.20	*B*	11–16	5.9(1.1)
28 900	0.20	*B*	11–16	5.1(1.1)
28 990	0.20	*A*	0–18	5.5(0.6)
29 490	0.20	*A*	0–18	6.7(0.8)
29 916	0.10	*A*	2–13	8.2(0.9)
30 067	0.15	*A*	0–18	10.3(1.3)
30 096	0.10	*A*	2–13	10.3(1.3)
30 116	0.20	*A*	0–18	10.6(0.9)
30 116	0.20	*B*	12–25	11.6(1.4)
30 127	0.15	*A*	0–18	10.1(1.2)
30 167	0.15	*A*	0–18	9.2(0.8)
30 217	0.20	*A*	0–30	9.3(0.8)
30 217	0.20	*B*	9–21	9.4(1.3)
30 303	0.20	*A*	0–18	8.5(0.9)
30 616	0.10	*A*	2–17	5.7(0.6)
31 000	0.15	*A*	0–18	3.9(0.5)
31 500	0.15	*A*	0–18	3.9(0.5)
34 131	0.20	*A*	2–14	6.8(1.7)

[a] Time delay between ketene excitation and CO detection.
[b] $A = {}^{12}CH_2\,{}^{13}CO$ and $B = {}^{13}CH_2\,{}^{12}CO$.
[c] Range of J (^{12}CO and ^{13}CO) used in the calculation of the exchange yield.
[d] Yields are corrected for impurity contributions to the CO signal. The 95% confidence levels for precision are shown in parentheses.

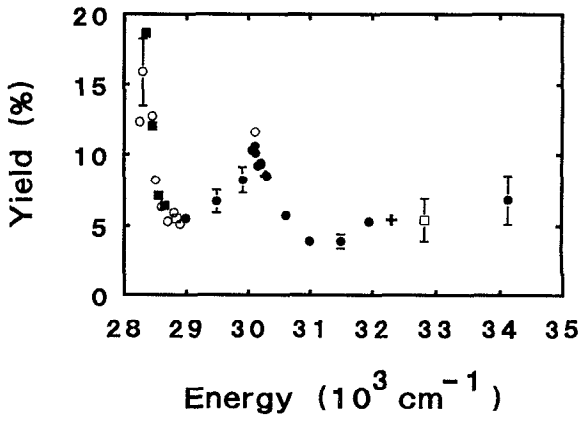

FIG. 5. Carbon atom exchange yield as a function of the ketene excitation energy. (○) $^{13}CH_2\,^{12}CO$ pulsed-jet/VUV LIF; (●) $^{12}CH_2\,^{13}CO$ pulsed-jet/VUV LIF; (■) pulsed-jet/VUV LIF, ^{12}CO and ^{13}CO kinetics ($^{13}CH_2\,^{12}CO$); (□) excimer photolysis/transient IR absorption; (+) low pressure (< 10 Torr) gas cell measurements by Russell and Rowland (Ref. 3) with $^{14}CH_2CO$. All the gas cell excitation energies have been adjusted for an average ketene internal energy of 350 cm^{-1} at 300 K. The error bars correspond to the 95% confidence limits for precision.

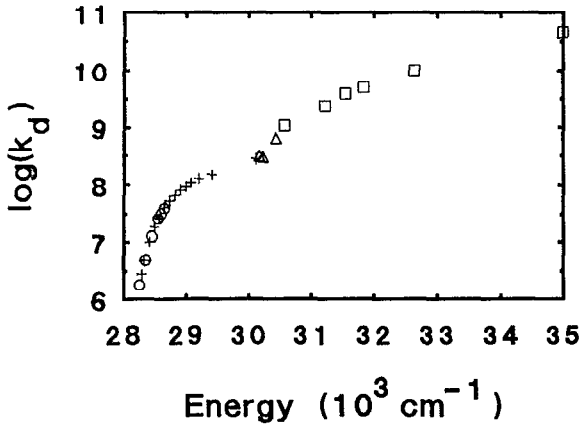

FIG. 6. Ketene unimolecular decomposition rate constant as a function of energy. (+) measurements of the appearance of the CO product by Chen and Moore (Ref. 20). (□) measurements of the appearance of the CH_2 ($a\,^1A_1$) (0,0,0) product by Potter *et al.* (Ref. 17). (○) measurements of the appearance of ^{12}CO and ^{13}CO following $^{13}CH_2\,^{12}CO$ excitation in this work. (△) singlet/triplet yield measurements by Kim *et al.* (Ref. 29).

energy in Fig. 6. The energy dependence of the exchange yield measured in this work exhibits a sharp local maximum at the singlet decomposition threshold energy, coincident with the pronounced step in the ketene decomposition rate constant. This correlation is consistent with a mechanism involving competition between ketene isomerization and decomposition. Below the singlet threshold, the decomposition rate constant is nearly independent of energy, which, accompanied by a steady increase in the isomerization rate, leads to an increase in the exchange yield with energy. At the singlet threshold, the decomposition rate increases rapidly and the fraction of molecules which isomerize drops, causing a decrease in the carbon atom exchange yield.

The competition between isomerization and decomposition is described more quantitatively with the following simple reaction mechanism.

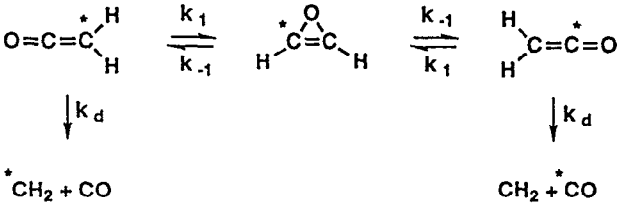

(16)

Equation (16) is consistent with the *ab initio* results for the isomerization mechanism (see Fig. 1).

In the statistical limit, the ratio of the oxirene formation and decomposition rate constants is

$$\frac{k_1(E)}{k_{-1}(E)} = \frac{\rho_{\text{oxirene}}(E)}{\rho_{\text{ketene}}(E)}, \tag{17}$$

where $\rho(E)$ is the density of states at energy E. Calculations of the vibrational state densities using the Whitten Rabinovitch approximation,[35] show that $k_1(E)/k_{-1}(E)$ is less than 10^{-4} over the range of energies examined in this study (28 250 to 34 100 cm^{-1}). Vibrational frequencies for the ketene ground electronic state were taken from experimental values[36] and oxirene frequencies were obtained from the *ab initio* calculations by Vacek *et al.*[8]

If the fraction of molecules in the oxirene form is very small, as predicted by Eq. (17), the reaction mechanism can be simplified further to

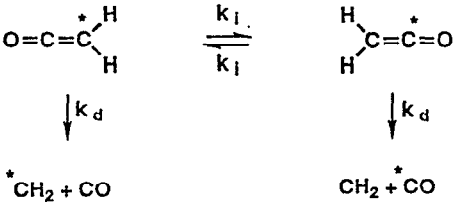

(18)

Equation (18) is based on the assumption that the isomerization and decomposition rate constants for $^{12}CH_2\,^{13}CO$ and $^{13}CH_2\,^{12}CO$ are the same. This treatment does not introduce any significant systematic errors since the reaction threshold energies for the two isotopomers are very similar (see Table II).

The production of *CO from ketene impurities must also be included in the reaction mechanism in order to make an accurate comparison with experimental results. The most important impurities in the $^*CH_2CO$ sample are $CH_2{}^*CO$ and $^*CH_2{}^*CO$ since they give high yields (> 80%) of *CO.

$$CH_2{}^*CO + h\nu \rightarrow CH_2 + {}^*CO, \tag{19}$$

$$^*CH_2{}^*CO + h\nu \rightarrow {}^*CH_2 + {}^*CO. \tag{20}$$

Here, it is assumed that $k_{19} = k_{20} = k_d$, which is justified since the impurity levels are low (1–2%) and the kinetic isotope effects are small (see Table II). Integration of the rate equations for the mechanism involving reactions (18), (19), and (20) results in the following relationships for the CO products.

$$[{}^*CO] = [{}^*CH_2CO]_0\{(I+0.5)(1-\exp(-k_d t) - C(1-\exp(-(2k_i+k_d)t)\}, \tag{21}$$

$$[CO] = [{}^*CH_2CO]_0\{0.5(1-\exp(-k_d t) + C(1-\exp(-(2k_i+k_d)t)\}, \tag{22}$$

$$[{}^*CO] + [CO] = [{}^*CH_2CO]_0(I+1) \times (1-\exp(-k_d t)), \tag{23}$$

where

$$C = \frac{k_d}{2(2k_i+k_d)}. \tag{24}$$

$[{}^*CH_2CO]_0$ is the concentration of the excited ketene isotopomer at time zero, and I is related to the purity of the reactant sample.

$$I=\frac{[CH_2{}^*CO]_0+[{}^*CH_2{}^*CO]_0}{[{}^*CH_2CO]_0}. \quad (25)$$

Combining Eqs. (21) and (22) gives an expression for the carbon atom exchange yield as a function of time.

$$Y=\frac{[{}^*CO]}{[{}^*CO]+[CO]}$$
$$=\{(I+0.5)(1-\exp(-k_dt)$$
$$-C(1-\exp(-(2k_i+k_d)t)\}/$$
$$(I+1)(1-\exp(-k_dt)). \quad (26)$$

Equation (26) shows that the exchange yield increases monotonically with time towards a limiting asymptotic value given by

$$Y(t\to\infty)=\frac{1}{I+1}\left\{I+\frac{k_i}{2k_i+k_d}\right\}. \quad (27)$$

The intercept of the yield vs time profile is determined by the level of impurity in the sample.

$$Y(t=0)=I/(I+1). \quad (28)$$

Rearranging Eq. (27) gives a simple relationship for the isomerization rate constant (k_i) as a function of the ketene decomposition rate constant (k_d) and the asymptotic exchange yield ($Y_{t\to\infty}$).

$$k_i=\frac{k_d[Y_{t\to\infty}(I+1)-I]}{1-2[Y_{t\to\infty}(I+1)-I]}. \quad (29)$$

The isomerization rate constant k_i was calculated using Eq. (29) with values of k_d obtained from interpolation of the data shown in Fig. 6 and the carbon atom exchange yields measured in this work. The calculated isomerization rate constants are plotted as a function of energy in Fig. 7. The isomerization rate constant increases smoothly with increasing energy as expected for an elementary process.

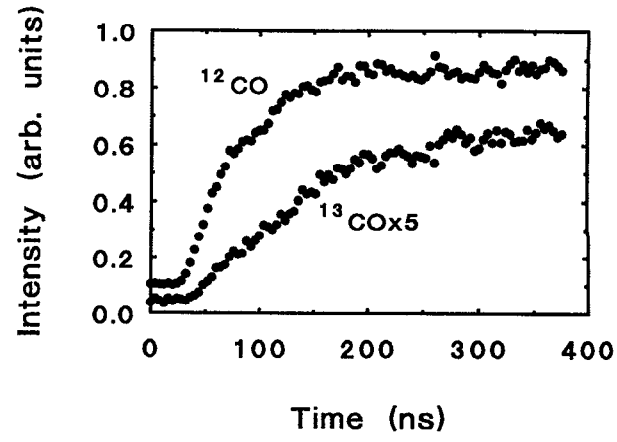

FIG. 8. Temporal profiles of ^{13}CO $Q(12)$ and ^{12}CO $Q(12)$ from the photolysis of $^{13}CH_2$ ^{12}CO at 28 450 cm^{-1}. The LIF intensity baselines are offset for clarity.

4. Isomerization kinetics experiments

The temporal evolution of both CO fragments was measured to test the simplified isomerization mechanism [reaction (18)]. The ^{12}CO and ^{13}CO rise profiles following $^{13}CH_2$ ^{12}CO excitation at 28 450 cm^{-1} are shown in Fig. 8. The time constant for the appearance of the minor ^{13}CO product is significantly longer than for the ^{12}CO product, as predicted by Eqs. (21) and (22). The time dependence of the yield of ^{13}CO for the same data set is shown in Fig. 9. The solid line is a nonlinear least-squares fit of the data to Eq. (26), giving $k_i=2.1\times10^6$ s^{-1}, $k_d=1.3\times10^7$ s^{-1}, and $I=0.018$.

The decomposition rate constant (k_d) was also measured by fitting the rise of the sum of the CO products to Eq. (23). The CO sum rise profile and a single exponential fit are

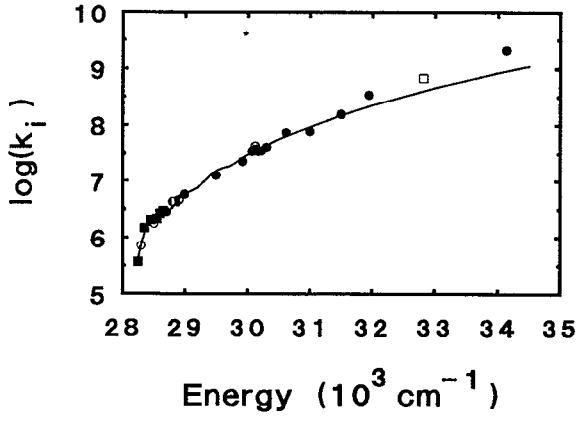

FIG. 7. Ketene isomerization rate constant as a function of excitation energy. The symbols have the same meanings as in Fig. 5. The solid line was calculated with tunneling-corrected RRKM theory using an oxirene transition state, a threshold energy of 28 360 cm^{-1}, and a barrier imaginary frequency of 400 i cm^{-1}. *Ab initio* harmonic frequencies of oxirene (Ref. 8) were used.

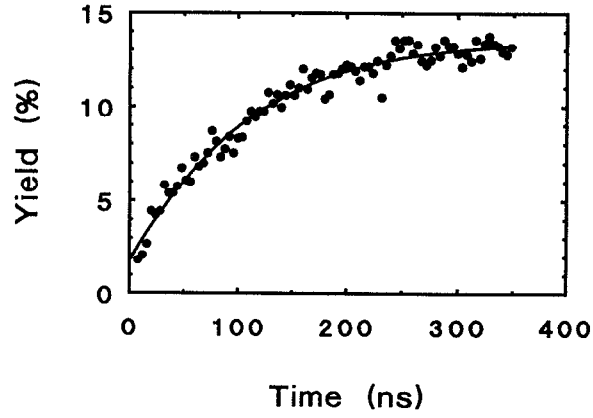

FIG. 9. Temporal evolution of the ^{13}CO yield from the photodissociation of $^{13}CH_2$ ^{12}CO at 28 450 cm^{-1}. The data are the same as shown in Fig. 8. The solid line is a nonlinear least-squares fit to Eq. (26) ($k_i=2.1\times10^6$ s^{-1}, $k_d=1.3\times10^7$ s^{-1}, and $I=0.018$).

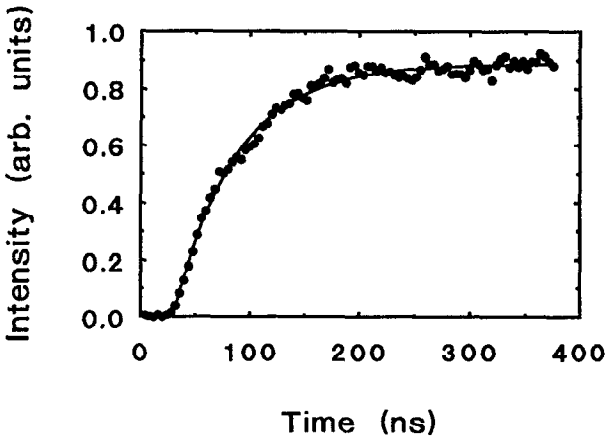

FIG. 10. The sum of $Q(12)$ LIF intensities of ^{13}CO and ^{12}CO as a function of time after excitation of $^{13}CH_2\,^{12}CO$ at 28 450 cm^{-1}. The data are the same as shown in Fig. 8. The solid line is a nonlinear least-squares fit to a single exponential rise [Eq. (23)] ($k_d = 1.7\times10^7\ s^{-1}$).

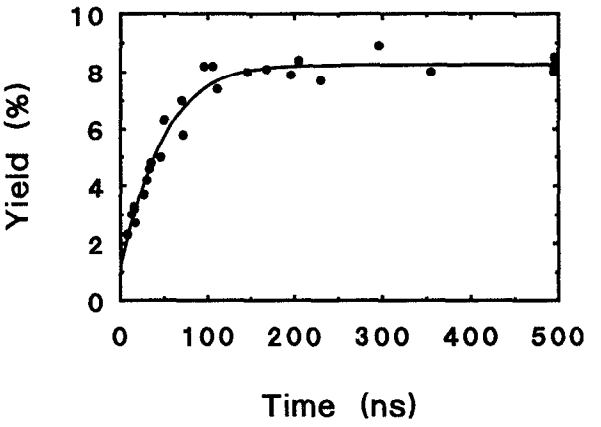

FIG. 11. The temporal evolution of the ^{13}CO yield from the photolysis of $^{13}CH_2\,^{12}CO$ at 28 600 cm^{-1}. Each data point was calculated from the integrated intensities of ^{12}CO $P(15)$ and ^{13}CO $Q(12)$ at a fixed time delay after ketene excitation. The solid line is a nonlinear least-squares fit of the data to Eq. (26) ($k_i = 2.7\times10^6\ s^{-1}$, $k_d = 3.2\times10^7\ s^{-1}$, and $I = 0.012$).

shown in Fig. 10. This fit gives $k_d = 1.7\times10^7\ s^{-1}$, which is in reasonable agreement with the result from a fit to the temporal evolution of the exchange yield for the same data set ($1.3\times10^7\ s^{-1}$).

The temporal evolution of the carbon atom exchange yield was also measured using a different experimental approach. In these experiments, the time delay between the excitation and the probe lasers was stepped manually, and at each step adjacent ^{12}CO and ^{13}CO LIF lines were scanned. The integrated intensities of the lines were converted to a yield by comparison with a complete analysis of ^{12}CO and ^{13}CO spectra at long reaction times. A yield temporal profile generated with this procedure is shown in Fig. 11. The solid line is a fit of the data to Eq. (26). All the isomerization and decomposition kinetic results are presented in Table IV. There is good agreement between the values of k_d determined from the fits of the rise of the sum of the CO products and the values from fits to the temporal evolution of the exchange yield. There is also good agreement between the kinetic parameters determined with the two different methods of measuring the temporal evolution of the exchange yield. The impurity levels are comparable with the concentration of $^{13}CH_2\,^{13}CO$ and $^{12}CH_2\,^{13}CO$ in the $^{13}CH_2\,^{12}CO$ sample obtained from FTIR spectra ($2\pm1\%$).

The decomposition rate coefficients (k_d) from the $^{13}CH_2\,^{12}CO$ kinetic experiments are plotted in Fig. 6 with the literature values for $^{12}CH_2\,^{12}CO$. There is good agreement for the two isotopomers (deviation $< \pm 30\%$) at all the energies except 28 250 cm^{-1}, where the decomposition rate constant of $^{13}CH_2\,^{12}CO$ is two times larger than the published value for $^{12}CH_2\,^{12}CO$. This comparison is based on linear interpolation of the $\log(k_d)$ vs E data for $^{12}CH_2\,^{12}CO$. The close agreement for the two isotopomers is consistent

TABLE IV. $^{13}CH_2\,^{12}CO$ isomerization and decomposition rate constants.[a]

Energy (cm^{-1})	Method[b]	k_i ($10^6\ s^{-1}$)	k_d ($10^6\ s^{-1}$)	Impurity (I)
28 650	I	3.0(15)	40(15)	0.020(12)
28 650	II		38(15)	
28 600	III	2.7(12)	32(11)	0.012(13)
28 550	I	2.2(5)	26(4)	0.020(6)
28 550	II		24(8)	
28 450	I	2.3(4)	15(3)	0.022(6)
28 450	II		15(4)	
28 450	III	1.8(8)	10(4)	0.023(21)
28 350	I	1.5(6)	4.9(9)	0.025(9)
28 350	II		3.5(9)	
28 250	III	0.31(8)	1.8(5)	0.012(9)

[a] The precision at the 95% confidence level based on three measurements is indicated in parentheses.

[b] Method I: probe laser fixed on the peak of $Q(12)$ and the time delay between ketene excitation and CO probe scanned. Yield vs time fit to Eq. (26). Method II: fit of the sum of ^{12}CO and ^{13}CO rise profiles to a single exponential rise [Eq. (23)]. Method III: time delay stepped and probe laser frequency scanned through adjacent ^{12}CO $P(16)$ and ^{13}CO $Q(12)$ peaks. Yield vs time fit to Eq. (26).

with the small dissociation threshold difference predicted by the zero point energy calculations shown in Table II. These calculations indicate that the threshold for triplet decomposition of $^{13}CH_2\,^{12}CO$ is about 20 cm^{-1} higher than that for $^{12}CH_2\,^{12}CO$. A 20 cm^{-1} energy difference corresponds to less than a 20% difference in the rate constants at energies above the threshold. However, at energies just below the $^{12}CH_2\,^{12}CO$ threshold, the decomposition rate of $^{13}CH_2\,^{12}CO$ should be up to 60% slower than that of $^{12}CH_2\,^{12}CO$, which is not observed experimentally. The discrepancy is ascribed to a systematic error in the data analysis for the published decomposition rate constants. New measurements of the decomposition rate constant for $^{12}CH_2\,^{12}CO$ are in better agreement with the present predictions.

5. Comparison with RRKM theory

In this section, the results of RRKM calculations for the ketene isomerization rate constant (k_i) are presented and compared with the experimental isomerization rate constants extracted from the kinetics and yield data. The purpose of the RRKM calculations was to check the applicability of simple statistical rate theory and to determine the energy threshold for the isomerization process.

The microcanonical RRKM rate constant is given by

$$k(E) = \frac{N^*(E)}{h\rho(E)}, \tag{30}$$

where $N^*(E)$ is the number of states at the transition region with energy less than or equal to E.[37] $\rho(E)$ is the density of reactant states at energy E, and h is Planck's constant. In this work, Miller's tunneling-corrected RRKM theory[38] was used, and $N^*(E)$ is given by the sum of Eckart tunneling probabilities over all states at the transition state.

Chen and Moore[20] have used the same tunneling-corrected RRKM theory to calculate decomposition rate constants of triplet ketene. They counted transition state vibrational states using *ab initio* vibrational frequencies calculated by Allen and Schaefer.[33] The RRKM rate constants were about twice the experimental rate constants in the threshold region, and showed greater deviations at higher energies. A fit of the experimental data gave the threshold energy (28 300 cm^{-1}), the imaginary frequency of the barrier (150 $i\,cm^{-1}$), and a correction factor for the ketene state density (a factor of 2). The overestimation of the decomposition rate constant by RRKM theory for energies >500 cm^{-1} above threshold was attributed to a rate limiting ISC rate constant of 3×10^8 s^{-1} or a transition state which required a variational treatment.

The theoretical calculations for the ketene isomerization suggest that there may be one transition state separating ketene and oxirene (see Fig. 1), although the stability of oxirene is still uncertain. Transition state force fields have not been reported and RRKM calculations based on an *ab initio* reaction coordinate are not feasible. However, the barrier between oxirene and ketene is expected to be small, and oxirene may be the dominant bottleneck in the carbon atom exchange process.

Ab initio vibrational frequencies for oxirene have been reported, and RRKM calculations were performed using an oxirene transition state. Oxirene states were counted using the highest level *ab initio* vibrational frequencies calculated recently by Vacek *et al.*[8] These calculations were performed with the single and double excitation coupled cluster (CCSD) method using a double zeta plus (DZP) basis set. The in-plane ring deformation mode (b_2) was treated as the reaction coordinate, and anharmonicities were not included in the oxirene state count. The ketene density of states was calculated with the Whitten–Rabinovitch[35] approximation and ground state vibrational frequencies.[36] The $\log(k_i)$ vs energy data was fit to the RRKM formalism with the threshold energy, the barrier imaginary frequency, and a multiplicative factor for the ketene density of states as variable parameters. The best fit ($E<29\,000$ cm^{-1}, $J=0$) gave a threshold energy of 28 360 $\pm$ 60 cm^{-1}, a barrier imaginary frequency of 400 $\pm$ 200 i cm^{-1}, and a correction factor for the ketene density of states equal to 0.9 $\pm$ 0.2. The quoted errors are 95% confidence limits based on estimated uncertainties ($\pm\sigma$) of $\pm$25% for the isomerization rate constants. The RRKM rate constants calculated with the threshold fit parameters are shown with the experimental data in Fig. 7. There is excellent agreement between the RRKM rate constant and the experimental isomerization rate constant for most of the energy range studied with essentially no modification to the ketene density of states.

IV. SUMMARY

(1) Isomerization reactions of highly vibrationally excited ketene lead to carbon atom exchange within the molecule. The isomerization processes compete effectively with unimolecular dissociation and produce significant yields (up to 20%) of *CO (CO) following excitation of $^*CH_2CO$ ($CH_2{}^*CO$).

(2) The yield for carbon atom exchange in ketene exhibits pronounced structure as a function of the excitation energy, with maxima at the triplet and singlet decomposition threshold energies.

(3) The time constant for the appearance of the exchanged CO fragment (e.g., *CO from $^*CH_2CO$) is significantly longer than the time constant for the appearance of the direct decomposition product (e.g., CO from $^*CH_2CO$).

(4) The rotational distributions of both CO products are the same, indicating that the exchanged CO dissociates from highly vibrationally excited ketene, and not from one of the other C_2H_2O isomers involved in the isomerization mechanism.

(5) A simple ketene isomerization mechanism [reaction (18)] describes the kinetics of the CO and *CO appearance, the energy dependence of the exchange yield, and the CO and *CO rotational distributions.

(6) Analysis of the CO and *CO kinetics and the carbon atom exchange yields gives the isomerization rate constant (k_i) as a function of energy.

(7) RRKM calculations using an oxirene transition state are in quantitative agreement with the experimental isomerization rate constant (k_i) for most of the energy range studied.

(8) A fit of the isomerization rate constant to tunneling-corrected RRKM theory gives a threshold for the isomerization process ($28\,360\ cm^{-1} \approx 81\ kcal\ mol^{-1}$), which is in good agreement with the *ab initio* oxirene energy.

ACKNOWLEDGMENTS

The authors are grateful to Young S. Choi for valuable assistance during the early stages of the pulsed-jet experiments. Charles D. Pibel, Roger D. Van Zee, and Miguel Rodriguez are thanked for many helpful discussions and technical assistance. The authors are also grateful to G. Vacek, B. T. Colegrove, and H. F. Schaefer III for the communication of their results prior to publication. S. K. K. acknowledges support from the University of California in the form of a Dora Garibaldi Scholarship, and R. A. A. is grateful to the U.S. National Science Foundation for a predoctoral fellowship. This work was supported by the Director, Office of Energy Research, Office of Basic Energy Sciences, Chemical Sciences Division of the U.S. Department of Energy under Contract No. DE-AC03-76SF00098.

[1] M. Torres, E. M. Lown, H. E. Gunning, and O. P. Strausz, Pure Appl. Chem. **52**, 1623 (1980).
[2] E. G. Lewars, Chem. Rev. **83**, 519 (1983).
[3] R. L. Russell and F. S. Rowland, J. Am. Chem. Soc. **92**, 7508 (1970).
[4] D. C. Montague and F. S. Rowland, J. Am. Chem. Soc. **93**, 5381 (1971).
[5] K. P. Zeller, Tetrahedron Lett. **8**, 707 (1977).
[6] W. J. Bouma, R. H. Nobes, L. Radom, and C. E. Woodward, J. Org. Chem. **47**, 1869 (1982).
[7] K. Tanaka and M. Yoshimine, J. Am. Chem. Soc. **102**, 7655 (1980).
[8] G. Vacek, B. T. Colegrove, and H. F. Schaefer III, Chem. Phys. Lett. **177**, 468 (1991).
[9] J. E. Del Bene, J. Am. Chem. Soc. **94**, 3713 (1972).
[10] C. E. Dykstra and H. F. Schaefer III, J. Am. Chem. Soc. **98**, 2689 (1976).
[11] W. D. Allen and H. F. Schaefer III, J. Chem. Phys. **84**, 2212 (1986).
[12] A. H. Laufer and R. A. Keller, J. Am. Chem. Soc. **93**, 61 (1971).
[13] R. N. Dixon and G. H. Kirby, Trans. Faraday Soc. **62**, 1406 (1966).
[14] M. Yoshimine, J. Chem. Phys. **90**, 378 (1989).
[15] I.-C. Chen, W. H. Green, Jr., and C. B. Moore, J. Chem. Phys. **89**, 314 (1988).
[16] W. H. Green, Jr., A. J. Mahoney, Q.-K. Zheng, and C. B. Moore, J. Chem. Phys. **94**, 1961 (1991).
[17] E. D. Potter, M. Gruebelle, L. R. Khundkar, and A. H. Zewail, Chem. Phys. Lett. **164**, 463 (1989).
[18] S. J. Klippenstein and R. A. Marcus, J. Chem. Phys. **91**, 280 (1989).
[19] I.-C. Chen and C. B. Moore, J. Phys. Chem. **94**, 269 (1990).
[20] I.-C. Chen and C. B. Moore, J. Phys. Chem. **94**, 263 (1990).
[21] D. C. Darwin, A. T. Young, H. S. Johnston, and C. B. Moore, J. Phys. Chem. **93**, 1074 (1989).
[22] E. R. Lovejoy, R. A. Alvarez, and C. B. Moore, Chem. Phys. Lett. **174**, 151 (1990).
[23] C. Chackerian, Jr., G. Guelachvili, and R. H. Tipping, J. Quantum Spectrosc. Radiat. Transfer **30**, 107 (1983).
[24] D. J. Nesbitt, H. Petek, M. F. Foltz, S. V. Filseth, D. J. Bamford, and C. B. Moore, J. Chem. Phys. **83**, 223 (1985).
[25] T. J. Buttenhoff, K. L. Carleton, and C. B. Moore, J. Chem. Phys. **92**, 377 (1990).
[26] R. Hilbig and R. Wallenstein, IEEE J. Quantum Electron. **17**, 1566 (1981).
[27] T. Bohland, F. Temps, and H. Gg. Wagner, Ber. Bunsenges. Phys. Chem. **88**, 455 (1984).
[28] C. C. Hayden, D. M. Neumark, K. Shobatake, R. K. Sparks, and Y. T. Lee, J. Chem. Phys. **76**, 3607 (1982).
[29] S. K. Kim, Y. S. Choi, C. D. Pibel, Q.-K. Zheng, and C. B. Moore, J. Chem. Phys. **94**, 1954 (1991).
[30] A. O. Langford, H. Petek, and C. B. Moore, J. Chem. Phys. **78**, 6650 (1983).
[31] C. H. Greene and R. N. Zare, J. Chem. Phys. **78**, 6741 (1983).
[32] P. D. Mallinson and L. Nemes, J. Mol. Spectrosc. **59**, 470 (1976).
[33] W. D. Allen and H. F. Schaefer III, J. Chem. Phys. **89**, 329 (1988).
[34] M. Hallman and I. Laulicht, Astrophys. J. Suppl. No. 110, **12**, 307 (1966).
[35] G. Z. Whitten and B. S. Rabinovitch, J. Chem. Phys. **38**, 2466 (1963).
[36] C. B. Moore and G. C. Pimentel, J. Chem. Phys. **38**, 2816 (1963).
[37] P. J. Robinson and K. A. Holbrook, *Unimolecular Reactions* (Wiley, New York, 1972).
[38] W. H. Miller, J. Am. Chem. Soc. **101**, 6810 (1979).